

Journal Pre-proof

Fe doped porous triazine as efficient electrocatalysts for the oxygen reduction reaction in acid electrolyte

Álvaro García, María Retuerto, Carlota Dominguez, Laura Pascual, Pilar Ferrer, Diego Gianolio, Aida Serrano, Pia Assmann, Daniel G. Sanchez, Miguel A. Peña, Sergio Rojas



PII: S0926-3373(19)31253-6
DOI: <https://doi.org/10.1016/j.apcatb.2019.118507>
Reference: APCATB 118507

To appear in: *Applied Catalysis B: Environmental*

Received Date: 31 July 2019
Revised Date: 8 November 2019
Accepted Date: 1 December 2019

Please cite this article as: García Á, Retuerto M, Dominguez C, Pascual L, Ferrer P, Gianolio D, Serrano A, Assmann P, Sanchez DG, Peña MA, Rojas S, Fe doped porous triazine as efficient electrocatalysts for the oxygen reduction reaction in acid electrolyte, *Applied Catalysis B: Environmental* (2019), doi: <https://doi.org/10.1016/j.apcatb.2019.118507>

This is a PDF file of an article that has undergone enhancements after acceptance, such as the addition of a cover page and metadata, and formatting for readability, but it is not yet the definitive version of record. This version will undergo additional copyediting, typesetting and review before it is published in its final form, but we are providing this version to give early visibility of the article. Please note that, during the production process, errors may be discovered which could affect the content, and all legal disclaimers that apply to the journal pertain.

© 2019 Published by Elsevier.

Fe doped porous triazine as efficient electrocatalysts for the oxygen reduction reaction in acid electrolyte

Álvaro García,¹ María Retuerto,^{1,*} Carlota Dominguez,¹ Laura Pascual,² Pilar Ferrer,³ Diego Gianolio,³ Aida Serrano,⁴ Pia Assmann,⁵ Daniel G. Sanchez,⁵ Miguel A. Peña,¹ Sergio Rojas^{1,*}

¹Grupo de Energía y Química Sostenibles, Instituto de Catálisis y Petroleoquímica, CSIC. Marie Curie 2, 28049, Madrid.

²Instituto de Catálisis y Petroleoquímica, CSIC. Marie Curie 2, 28049, Madrid, Spain.

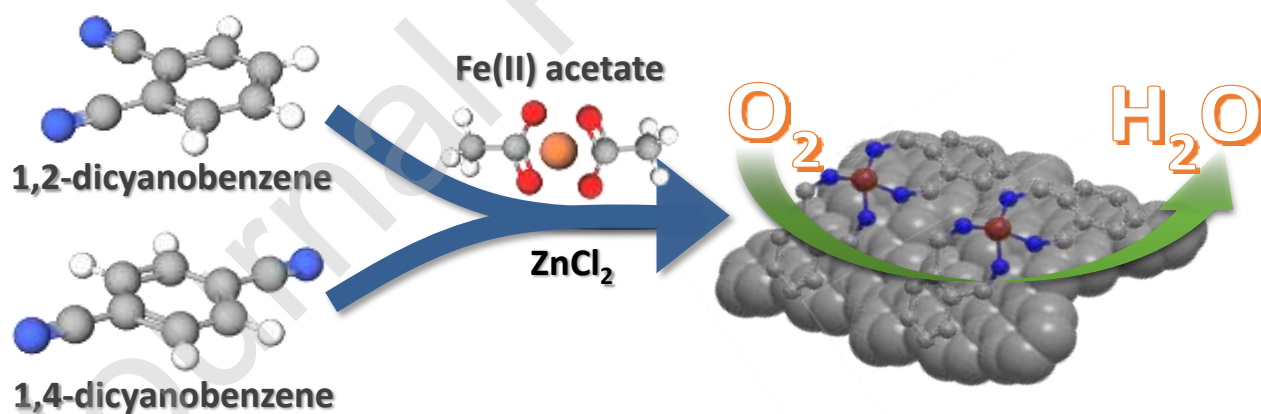
³Diamond Light Source, Harwell Science and Innovation Campus, Chilton, Didcot OX11 0DE, United Kingdom

⁴SpLine, Spanish CRG BM25 Beamline at The European Synchrotron, 71 Avenue des Martyrs, 38000 Grenoble, France

⁵German Aerospace Center (DLR), Institute of Engineering Thermodynamics, Pfaffenwaldring 38-40, 70569 Stuttgart, Germany

Corresponding author: srojas@icp.csic.es

Graphical abstract



Highlights

- Novel Fe/N/C electrocatalysts for Oxygen Reduction Reaction (ORR) in acid media based in porous organic polymer precursors using non-expensive 1,2- or 1,4- dicyanobenzene (DCB) and iron-based starting materials.

- The nature of the starting materials affects the ORR activity, being more active the catalysts using 1,2-DCB than 1,4-DCB, probably because vicinal positions of N-bearing groups are more prone to coordinate to one Fe atom to form the FeN_x moieties.
- The ORR activity is boosted by the presence of FeN_x moieties.

Abstract

In this work, we report the synthesis of Fe/N/C electrocatalysts using triazine based porous organic polymers as precursors. Iron-doped triazine porous organic polymers were obtained by in situ polymerization of iron precursor and 1,2- or 1,4- dicyanobenzene (DCB). In order to obtain the actual catalyst, the polymer obtained was subjected to thermal treatment under NH₃. The catalysts obtained exhibit activity and durability for the oxygen reduction reaction in acid electrolyte. Thorough characterization of the catalysts reveal the formation of several types of iron species, including metallic iron, iron carbides and Fe-N_x moieties. The latter species is the main responsible for the high activity measured for the oxygen reduction reaction in acid electrolyte. 1,2-DCB results in more active catalysts than 1,4-DCB due to the higher fraction of FeN_x ensembles in the former, probably because vicinal positions of N-bearing groups are more prone to coordinate Fe atoms.

Keywords: ORR; NPMC; Triazine; PEMFC; Fe-N

Introduction

Electrocatalytic processes are among the most promising technologies called to achieve a deep decarbonization of today's energy system. In particular, the electrochemical interconversion between H₂O and H₂/O₂ with the associated use and production of energy is the core of electrolyzers and fuel cells, respectively [1, 2]. However, those technologies are not mature for a large-scale penetration into the energy market [3, 4]. Low-temperature H₂-feed fuel cells generate direct electrical potential difference (work) by the recombination of O₂ and H₂ with the only bi-product of H₂O. The overall process is

limited by the sluggish kinetics of the oxygen reduction reaction (ORR), which even with the state-of-the-art Pt-based electrocatalysts only proceeds at measurable rates (current) if the potential is driven away from the equilibrium (overpotential). The benchmarking catalysts for Proton-Exchange Membrane Fuel Cells (PEMFCs) are based on nanosized Pt particles deposited onto high-area mesoporous carbon. High Pt loadings are used in order to overcome the sluggish kinetics of the ORR, typically between 22 and 40 g of platinum group metals/vehicle, being the catalyst almost half of the overall cost of the fuel cell stack [4, 5]. Therefore, it is of great technological and scientific significance to seek for alternative electrocatalysts based on earth-abundant nonprecious materials to replace Pt-based ones, especially at the acid pH required for the proton exchange through the membrane [6, 7]. The most promising Pt-free catalysts for the ORR are based on transition metals (typically Fe and/or Co) coordinated to N atoms in C-C sp^2 network [8-16]. In our group, we have recently reported a Fe/N/G electrocatalyst with high ORR activity and durability [17, 18]. A graphene-like matrix is used as the carbon matrix for the formation of FeN_x ensembles. This electrocatalyst shows mass activity of 2.03 A g^{-1} at 0.8 V vs. RHE in acidic solution [19].

A myriad of N, C and Fe precursors, and protocols for the synthesis of Fe/N/C catalysts have been proposed, see references [13, 20, 21]. Although many aspects of the synthesis of Fe/N/C remain elusive, certain common steps essential for obtaining highly active catalysts have been identified. Thus, the material obtained upon the mixing of the C, N and Fe precursors should be subjected to one or several thermal treatment(s) under inert (Ar, N_2) and/or reactive atmosphere (NH_3) to obtain the final catalysts. This thermal treatment results in the formation of different species, *e.g.*, FeN_x ensembles within the carbon matrix, iron carbides (Fe_3C , Fe_5C_2) or nitrides, metallic iron, iron oxides, defectively coordinated C atoms, and N-C ensembles with N atoms in different coordination (pyrrolic, pyridinic, quaternary...). In addition, thermal treatment under NH_3 results in the generation of (micro) porosity, ideally with N atoms (and FeN_x ensembles) in micropores, which endows the final material with high ORR activity [8, 11, 22, 23]. It should be noted, however, that the location of active sites in micropores results in mass transfer issues, especially at high current densities [24, 25].

A critical aspect of the synthesis of Fe/N/C is the actual nature of C, N, and Fe atoms during the thermal protocol since it is in this step when the FeN_x ensembles are formed. Using low-molecular high-volatile N and C precursors results in severe losses of the initial material (higher than 90%) during the pyrolysis step, *i.e.*, (extremely) low reaction

yields, which is critical when expensive N and C precursors are used. In addition, it has been reported that the durability of Fe/N/C catalysts increases with the degree of graphitization of the carbon matrix.[19] Therefore, it is reasonable to assume that using high molecular-weight thermally-stable C-N polymers with higher degree of graphitization would improve the stability of the Fe/N/C catalysts obtained. In fact, the most active Fe/N/C catalysts reported in the literature are based on high molecular weight structures, typically MOFs [11, 26], POPs [27] (porous organic polymers) or other polymers such as polyacronitrile [28], which contain a high population of N atoms within a porous carbon structure. The interested reader is referred to reference [29] for a comprehensive review of the most active Fe/N/C catalysts for the ORR reported in the literature. The final catalysts are obtained by co-pyrolysing the polymeric structure and the Fe precursor at high temperature.

Porous, covalent triazine frameworks, usually referred to as Triazine Porous Organic Polymers (TPOP) are a class of N-containing organic polymers with high surface area and a defined porous structure, which can be prepared by several precursors and methods [30, 31]. Recently, the use of TPOP as catalysts or catalyst precursors for the ORR has been reported by several authors [32-37]. The materials obtained were used as electrocatalysts for the ORR in alkaline, and to a lesser extent, in acid electrolyte after the incorporation of Fe or Co atoms. However, the synthesis of the TPOPs usually requires (very) expensive precursors and complicated, multistep synthetic procedures thus jeopardizing the scaling up of catalyst production. Kuhn et al. reported a simple and economic process for the synthesis of TPOP based upon the ionothermal polymerization of 1,4-dicyanobenzene (1,4-DCB) at 400°C in the presence of ZnCl₂ which results in the formation of high surface area, triazine polymers [38]. Whereas this TPOPs synthesized from 1,4-DCB have tested as photocatalysts for hydrogen evolution [39], to the best of our knowledge, neither the synthesis of TPOP using 1,2-DCB as starting material nor the possibility of incorporating Fe (or metallic) atoms *in situ* during the ionothermal polymerization of DCBs has been explored hitherto.

In this work, we report a one-pot synthesis of Fe/N/C catalysts based on TPOFs with high activity and durability for the ORR in acid electrolyte. The catalysts were prepared by polymerization under ionothermal conditions of 1,2-DCB or 1,4-DCB with ZnCl₂ at 400°C in the presence of Fe(C₂H₃O₂)₂ as iron source. The materials obtained were subjected to pyrolysis under NH₃-containing atmosphere and acid leaching to remove the

Fe soluble phases. The catalysts obtained display high surface area and high ORR activity and durability in acid electrolyte.

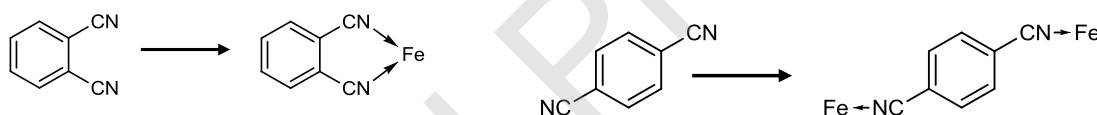
2. Experimental Section

2.1 Synthesis of catalysts

Unless otherwise stated, all chemicals were purchased from Sigma Aldrich and used as received. ZnCl_2 anhydrous was purchased from Alfa Aesar. The synthesis of the Fe/N/C catalysts is based on a modified method of the synthesis of porous triazine frameworks via the ionothermal polymerization of 1,4-DCB reported by Kuhn et al. [40]. In this work, we used two DCB isomers as C and N precursors, namely 1,2-DCB and 1,4-DCB, and conducted the polymerization reaction using zinc chloride as catalyst in the presence of iron acetate (II).

The polymerization of 1,4-DCB in the presence of ZnCl_2 leads to TPOP with high surface area. However, having the N-containing groups in 1,4 positions could the coordination of Fe atoms can be compromised. This issue can be minimized by using 1,2-DCB as precursor since the N-containing groups are located in vicinal positions, see scheme 1.

Scheme 1. Illustration of N-Fe coordination modes in 1,2-DCB and 1,4-DCB.



In a typical synthesis, 1,2-DCB or 1,4-DCB, ZnCl_2 and iron acetate were mixed in a glove box in a 1:1 DCB: ZnCl_2 and 1:4 Fe:N (in DCB) molar ratios. The Fe:N ratio was selected in order to boost the formation of FeN_4 ensembles. The mixing was sealed under vacuum conditions in a Pyrex vial. Then the mixture was heat-treated in a furnace for 46 hours at 400 °C. The resultant monoliths were ball-milled (planetary) for 60 min in a stainless-steel vessel, recovered and subjected to a pyrolysis treatment at 900 °C for 30 minutes in NH_3/N_2 . The solids obtained after the first pyrolysis were named HT-1,2 and HT-1,4; when 1,2-DCB and 1,4-DCB are used as precursors, respectively.

After the pyrolysis, an acid leaching is needed in order to eliminate the Fe soluble phases in acid (for instance, metallic Fe). The acid leaching has been performed by dispersing the catalysts in a solution of 0.5 M H_2SO_4 at 60 °C and strong stirring for 2 hours. After

the acid leaching, a second pyrolysis treatment is performed using the same conditions than the first pyrolysis. The solids obtained were labelled as 2HT-1,2 and 2HT-1,4.

2.2 Catalyst Characterization

C, N, and H contents were determined by elemental analysis. Specific surface areas and pore size distribution was determined by the BET method. A Micromeritics ASAP 2000 apparatus was used for the measurements. Surface areas were evaluated from the adsorption/desorption nitrogen isotherms within the relative pressure range $P/P_0 = 0.05 - 0.30$. The amount of adsorbed nitrogen is related to the total surface area of the samples. The volume of gas adsorbed on the surface is measured at $-196\text{ }^{\circ}\text{C}$ (nitrogen boiling point). The samples are finally degassed at $140\text{ }^{\circ}\text{C}$ under vacuum for 24 h. X-ray Powder Diffraction (XRD) was performed in Bragg-Brentano reflection geometry with $\text{CuK}\alpha$ radiation ($\lambda = 1.5418\text{ \AA}$). Transmission Electron Microscopy (TEM) data was recorded on a JEOL 2100 field emission gun transmission electron microscope operating at 200 kV and equipped with an EDX spectrometer Oxford INCA Energy 2000 system. Specimens were prepared by depositing small portions of the samples on top of a Cu grid supporting a lacey carbon film. Deposition was achieved by preparing a suspension of the material in ethanol.

X-ray photoelectron spectra (XPS) were collected in a VG ESCALAB 200 R at a pass energy of 50 eV with a Mg $\text{K}\alpha$ X-ray source. The kinetic energies of the photoelectrons were measured using a hemispherical electron analyser working in the constant-pass energy mode. The background pressure of the analysis chamber was below 3×10^{-8} mbar. Around 200 scans were collected in increments of 0.1 eV with dwell times of 50 ms. C 1s peak at 284.8 eV was used to determine the binding energies (± 0.2 eV). The spectra were analysed with the CASA software. A Shirley type background was used. The peaks were adjusted to Gaussian/Lorentzian (30) line shape. The FWHM of the N 1s peaks was allow to vary between 1.8 and 2.4 eV.

Raman spectra were recorded using a single monochromator Renishaw system 1000 equipped with a thermoelectrically cooled CCD detector and holographic super-Notch filter. The spectra were recorded in air. The samples were excited with the 532 nm Ar line. The instrument is calibrated with a silicon reference at 520 cm^{-1} (resolution of 1 cm^{-1}). We recorded 5 spectra for each sample with an acquisition time of 10 s.

X-ray absorption spectroscopy (XAS) data at the Fe K-edge (7112 eV) were measured in the fluorescence yield mode at the Spanish beamline (SpLine CRG, BM25) of The

European Synchrotron (The ESRF), Grenoble. The electron beam energy of the ring was 6 GeV and the average current was 200 mA. The incident beam was monitored in an ionization chamber filled with N₂. Fe K_α fluorescence line was collected under a 90° geometry to the incident beam direction, using a 13-element Si(Li) detector from e2v Scientific Instruments. The energy was set using a double Si(1 1 1) crystal monochromator refrigerated at 200 K by a homemade ethanol cooling system, which was detuned up to a 70% of the maximum intensity to reject components from higher harmonics. A Fe foil was also measured to use it as reference. Several measurements were performed in order to assure a good signal-to-noise ratio and an average spectrum is presented for each sample. Data treatment and addition of spectra to improve the signal-to-noise ratio has been performed with the ATHENA software [41]. Fourier transform of k²-weighted $\chi(k)$ was performed with k-range from 2 to 11 Å⁻¹ for HT set of samples and from 2.5 to 8.5 Å⁻¹ for 2HT set of samples. Longer ranges for 2HT samples could not be used due to the low signal to noise ratio.

2.3 Electrochemical measurements

The electrochemical tests were conducted using an Autolab Pgstat 302 N potentiostat/galvanostat. We measured in a standard three-compartment glass cell with a rotating disk electrode (RDE) (Pine Research Instruments) as working electrode, a graphite bar and a homemade reversible hydrogen electrode (RHE) as counter and reference electrodes. To determine the formation of hydrogen peroxide, a Pt ring rotating disk electrode (RRDE) was used. The catalysts were deposited on a glassy carbon (GC) electrode by means of an ink. A mass of 6 mg of electrocatalyst, 780 µl Millipore MilliQ® water, 200 µl of isopropyl alcohol and 20 µl of 5 wt.% Nafion were mixed and ultrasonically dispersed to make the ink. A volume of 20 µl of the catalyst ink was deposited onto de GC electrode surface (0.196 cm²) giving a catalyst loading of 0.6 mg_{cat}/cm².

The ORR measurements were performed in O₂ saturated 0.1 M high purity HClO₄ at 10 mVs⁻¹ and 1600 rpm. Background currents were recorded under Ar-saturated electrolyte. Accelerated durability tests were performed by collecting 500 cycles at 50 mVs⁻¹ between 0.6 and 1.0 V vs. RHE in an Ar saturated electrolyte.

2.4 MEA testing

An MEA using the 2HT-DCB catalysts as cathode and Pt/C as anode was assembled by using the drop casting method. The GDL was fixed on a heating plate at 90°C under a fume hood. The catalysts were coated onto the GDL by means of an ink, using a precision syringe and a needle. The Ink was prepared via a one-pot reaction. Thus, 15 mg of the catalyst, 15 mg of Nafion-solution (5 wt.% in lower aliphatic alcohol and water from Sigma-Aldrich) and 2 mL of Ethanol (98% absolute from Sigma Aldrich) were mixed for 2h in an ultrasonic bath at 30-80°C. The catalyst to Nafion ration used was I/C=1 (50/50 wt.%). To avoid sedimentation, the solution should be shaking every 30 minutes.

3. Results and Discussion

3.1 Physicochemical characterization

The C, H, and N contents (wt.%) of the catalysts were determined by elemental analysis, see Table 1. The amount of N actually incorporated into the samples ranges between 1.3-1.6 wt.%. Before the acid treatment (HT samples) the carbon content of the catalysts is ~ 70 %, increasing to ~ 90 % after acid leaching and second pyrolysis. The increasing fraction of carbon in the 2HT catalysts accounts to the removal of the non-stable iron phases and of ZnCl₂ during the acid treatment (note that most ZnCl₂ is removed during the first pyrolysis step). As observed, the amount of N is slightly higher in the catalysts prepared with 1,2-DCB than with 1,4-DCB. The content of N increases after the acid treatment and second pyrolysis step in both catalysts. In addition, the specific surface areas of the catalysts, obtained by the BET method, are also reported in Table 1. Before pyrolysis, *i.e.*, after the first treatment at 400 °C, the BET surface area of the polymers is small, ~ 5 m²/g, indicating that the pyrolysis is necessary to produce high surface area catalysts. However, this value should be taken cautiously. For the correct evaluation of the surface area of the polymer obtained, the ZnCl₂ used for the polymerization should be removed from the solid. This process is usually conducted by acid leaching, a process that would lead to the removal of Fe soluble species, which is undesired at this point of the synthesis. Therefore, we decided not to perform acid leaching on the initial polymers and subject the solid obtained to a pyrolysis step. Most of the ZnCl₂ is removed during the thermal treatment. After the first pyrolysis, the surface specific areas of the HT samples are around 350 m²g⁻¹, increasing to 450-490 m²g⁻¹ after acid leaching and second pyrolysis (2HT samples). As observed in Table 1 both micropores and external areas increase with the second pyrolysis. The increase of the surface area after several pyrolysis treatments have been reported previously for other Fe/N/C catalysts [8].

Albeit the exact nature of the active sites for the ORR in Fe/N/C catalysts remains elusive, there is a large body of experimental and theoretical work that support that iron atoms, more specifically FeN₄ ensembles, are directly responsible for the high ORR activity in acid electrolyte, especially at low overpotentials [37, 42-45]. The presence of Fe and N has been demonstrated and quantified by chemical analysis. The exact nature of Fe and N atoms in the catalysts has been carefully analyzed by a combination of bulk and surface techniques.

Table 1: Elemental composition (wt.%), N/C ratio (atomic) and specific surface areas of the catalysts

Catalyst	*Weight content / %			N/C atomic ratio	**Specific surface area / m ² g ⁻¹	Pore distribution / nm
	C	N	H			
HT-1,2	69.72	1.48	0.73	0.025	316 (152/164)	3.7
HT-1,4	73.54	1.29	0.67	0.020	357 (152/205)	3.7
2HT-1,2	88.66	1.61	0.81	0.021	448 (217/231)	3.6
2HT-1,4	90.58	1.45	0.80	0.019	485 (232/253)	3.7

*The rest is Fe and O in the catalysts. **Specific surface areas determined from the BET method. The values in parentheses indicate micropore/external areas.

Figure 2 shows the XRD patterns of HT and 2HT samples. After the first thermal treatment in NH₃/N₂ the diffractograms of HT-1,2 and HT-1,4 display diffraction lines of reduced iron species (metallic Fe and Fe₃C) and carbon, in line with the reducing conditions of the pyrolysis. Diffraction lines for iron oxides, ZnCl₂ or other Zn species are not observed in the diffractograms.

Metallic Fe and Fe₃C phases solubilize during PEMFC operation so they have to be removed from the catalysts before use. This process is usually conducted by acid treatment, see section 2.1. After the acid leaching and the second thermal treatment in NH₃/N₂ the only reflections observed in the 2HT catalysts are a strong one at 25 °C corresponding to the (002) planes of graphitic carbon and a set of ill-defined reflections at ca. 45 ° corresponding to Fe₃C. XRD results indicate that metallic iron and most of the Fe₃C phases are dissolved during the acid leaching. As shown below, the Fe₃C particles remaining in 2HT-1,2 and 2HT-1,4 are Fe₃C particles wrapped within several layers of graphitic carbon that prevent them from dissolve during the acid leaching.

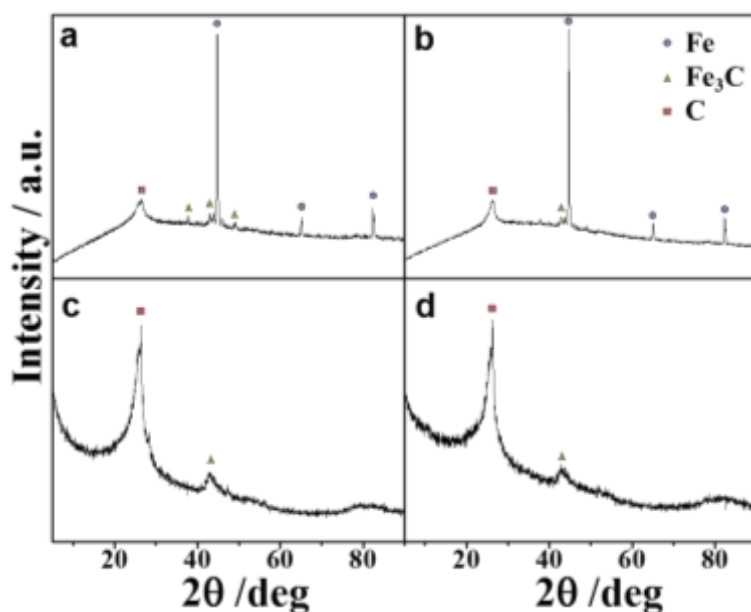


Figure 1: XRD patterns of a) HT-1,2; b) HT-1,4; c) 2HT-1,2; and d) 2HT-1,4.

The composition, morphology, and structure of the catalysts have been further analyzed by TEM.

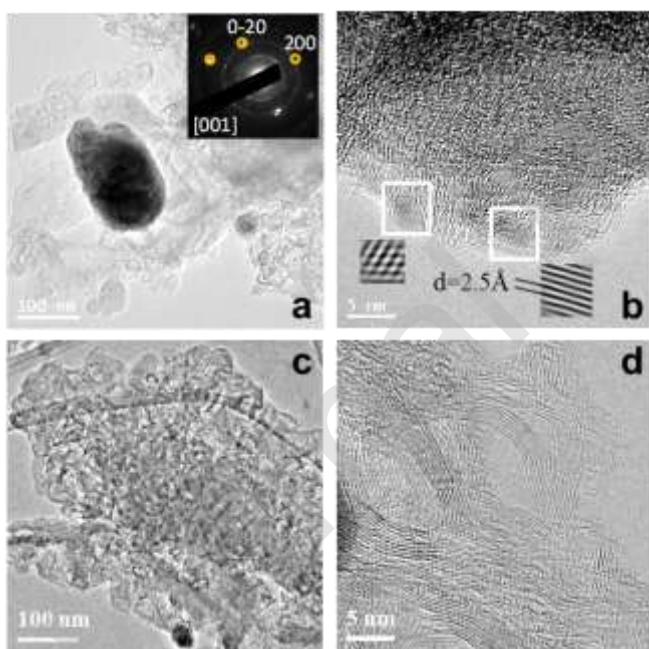


Figure 2: (a) TEM micrograph of HT-1,2 showing Fe metallic particles (the inset is a SAED of one Fe particle along the [001] zone axis) and (b) HRTEM of HT-1,2 showing FeO_x nanoparticles in the carbon matrix, (c) TEM image of 2HT-1,2 and (d) HRTEM of the same sample showing higher degree of carbon crystallization than HT samples.

As observed in Figure 2a, HT-1,2 presents a carbon matrix in which metallic Fe particles and Fe₃C are observed. The size of the Fe₃C particles ranges between 10 and 30 nm,

although a small fraction of Fe particles larger than 100 nm can be observed. An analysis of the catalysts by electron diffraction (SAED) indicates that the ~100 nm Fe particles are actually metallic Fe. The inset of Figure 2a shows a representative SAED pattern of one of the particles, which can be indexed as the [001] zone axis of a cubic metallic Fe structure. Figure 2b shows a HRTEM image of the carbon matrix where iron-rich nanoparticles of 3-5 nm can be observed. The measured interplanar distance of $d = 2.5 \text{ \AA}$ suggests that these particles are iron oxide. The analysis of the samples subjected to acid leaching and second pyrolysis (2HT samples) reveals a major transformation of the catalysts. Figure 2c shows a representative TEM micrograph of 2HT-1,2. The large Fe metallic particles (larger than 100 nm) have disappeared, and only a small fraction of the 10-30 nm particles is still observed (Figure 2c). The HRTEM micrograph shown in Figure 2d reveals a high degree of graphitization of the carbon matrix and the absence of Fe oxide nanoparticles, in contrast with the nanoparticles observed in HT-1,2 (Figure 2b).

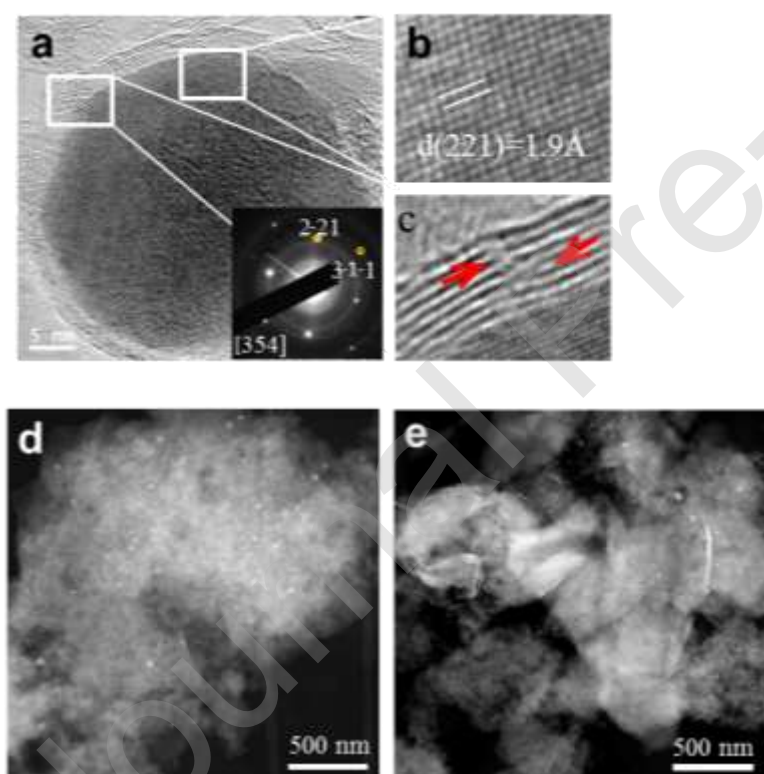


Figure 3: (a) HRTEM of a Fe₃C particle wrapped by graphite layers. Inset: corresponding SAED pattern oriented along the [354] zone axis of the cohenite structure. (b) HRTEM magnification of an area of Fe₃C and (c) detail of the graphite layers around Fe₃C, showing dislocations (arrowed). (d) STEM image of HT-1,2 (e) STEM image of 2HT-1,2.

The 10-30 nm nanoparticles in HT-1,2 and 2HT-1,2 have been further analyzed by HRTEM. Figure 4a and b show a representative HRTEM image at high magnifications

of one of these particles. The SAED pattern in the inset can be indexed as the [345] zone axis of Fe_3C with the cohenite structure (inset Figure 3a). However, comparing the STEM-HAADF images of HT (Figure 3d) and 2HT (Figure 3e), reveals that a high fraction of the Fe_3C particles have been dissolved with the acid leaching and the STEM images for the 2HT samples show a lower content of these particles. The remaining Fe_3C particles in 2HT are wrapped within several (8-20) layers of carbon (Figure 3c). These carbon layers avoid the dissolution of encapsulated Fe_3C during the acid leaching. A close inspection of the carbon layers encapsulating the Fe_3C particles present defects such as dislocations, see Figure 3c, that are expected to result a high degree of strain of such graphite layers. The dislocations could be related to the presence of Fe and/or N atoms at the edges of the graphite layers. In conclusion, TEM results confirm that the leaching and the pyrolysis processes result in the removal of metallic Fe, Fe oxide nanoparticles and a fraction of Fe_3C , in particular Fe_3C that is not encapsulated within graphitic carbon.

The surface composition of the catalysts was analyzed by XPS. Table 2 shows the surface atomic abundance of C, N, and Fe atoms for each sample. As shown in Table 2 the catalysts synthesized from 1,2-DCB and 1,4-DCB display similar N/C atomic ratios. As also observed in Table 2, the actual N/C ratio slightly decreases after the second pyrolysis step for both set of catalysts. This observation is in good agreement with the bulk N/C contents obtained by chemical analysis and suggests a homogeneous distribution of C and N in the catalysts. Sample HT-1,2 displays a lower Fe/N and Fe/C atomic ratio than HT-1,4. In addition, the Fe/N and Fe/C ratios of the catalysts subjected to acid leaching and second pyrolysis (2HT- series) are smaller than those of the corresponding HT-samples. The XPS Fe 2p region presents a small Fe $2p_{3/2}$ peak centered at ca. 710 eV for all catalysts, see Figure 4a. This binding energy is characteristic of Fe oxidized species. The spectra of iron oxides are characterized by the presence of shake-up satellite peaks that appear at higher binding energies than that of the main photoelectronic peak. The position of these satellite peaks is used to discriminate whether the main peak accounts to Fe^{2+} and/or Fe^{3+} species. However, no distinct shake up peaks can be observed in the spectra of the core-level region of Fe in the samples under study, especially in the 2HT catalysts, suggesting that the Fe species responsible for the main peak at ca. 710 eV in the 2HT-catalysts are not iron oxides but oxidized Fe atoms coordinated to N atoms. Nevertheless, due to the low intensity of the peaks the presence of the satellite peaks cannot be ruled out completely.

On the other hand, evidences of the presence of metallic iron are not observed in the spectra of the Fe core-level region. This observation is in striking contrast with the XRD data that reveal the presence of metallic iron (in the HT samples) and iron carbides (HT and 2HT samples). This feature can be explained by taking into account that iron carbides are wrapped by several graphite layers that prevent their observation by a surface sensitive technique such as XPS; and metallic Fe in HT samples is not observed since it is oxidized in the surface of the catalysts, generating the peaks characteristic of Fe oxidized. In fact, Fe-O nanoparticles in the surface of HT samples are observed by TEM (see above).

As observed in Table 2, the Fe surface content in both HT samples is higher than in 2HT. This trend is in good agreement with the expected removal of Fe during acid leaching. As also observed in Table 2, HT-1,4 losses more Fe during the acid leaching than HT-1,2; a feature that explains the catalytic activity of these samples for the ORR before and after the acid leaching (see below).

Table 2. Surface Fe, N, and C atomic ratios and percentage of N-species obtained by XPS.

	HT-1,2	HT-1,4	2HT-1,2	2HT-1,4
Fe/N (at/at)	0.044	0.064	0.032	0.038
N/C (at/at)	0.024	0.025	0.021	0.018
Fe/C (at/at)	0.0011	0.0016	0.0007	0.0007
O/C (at/at)	0.071	0.075	0.108	0.072
N-pyridinic (%)	23	22	19	16
FeN _x (%)	14	7	10	10
N-Pyrrolic (%)	49	50	45	53
N-Graphitic (%)	6	13	18	14
N-Oxides (%)	8	8	8	7

It is well established that Fe/N/C catalysts present N atoms in different configurations and the ORR activity of the catalysts is determined by the fraction of N atoms in each configuration. In particular, it has been reported that pyridinic N promotes the four-electron pathway (direct reduction of $O_2 \rightarrow H_2O$) as compared to N-graphitic which is claimed to promote the two-electron pathway ($O_2 \rightarrow H_2O_2$) [42, 46, 47]. However, it is also well established that the most active sites for the ORR are constituted by iron (or transition metals) coordinated to N atoms, namely FeN_x [42, 43], especially FeN₄ moieties hosted at edge sites [48].

The analysis of the N species in Fe/N/C catalysts is usually conducted by XPS. Figure 4a shows the N 1s core-level spectra of the samples under study. As observed, the spectra for all catalysts are similar showing peak maxima at ca. 401 eV and a shoulder to lower binding energies. In fact, the main difference between the spectra is the intensity of the shoulder which seems to be the highest for HT-1,2. The N 1s core-level region of the catalysts has been analyzed in detail by deconvolution of the spectra into five components at ca. 398.4, 399.2, 400.7, 402.6, and 405.6 eV. The peaks are ascribed to pyridinic N, N coordinated to Fe (Fe-N_x), pyrrolic N, graphitic and/or N quaternary and N oxidized, respectively [42, 49].

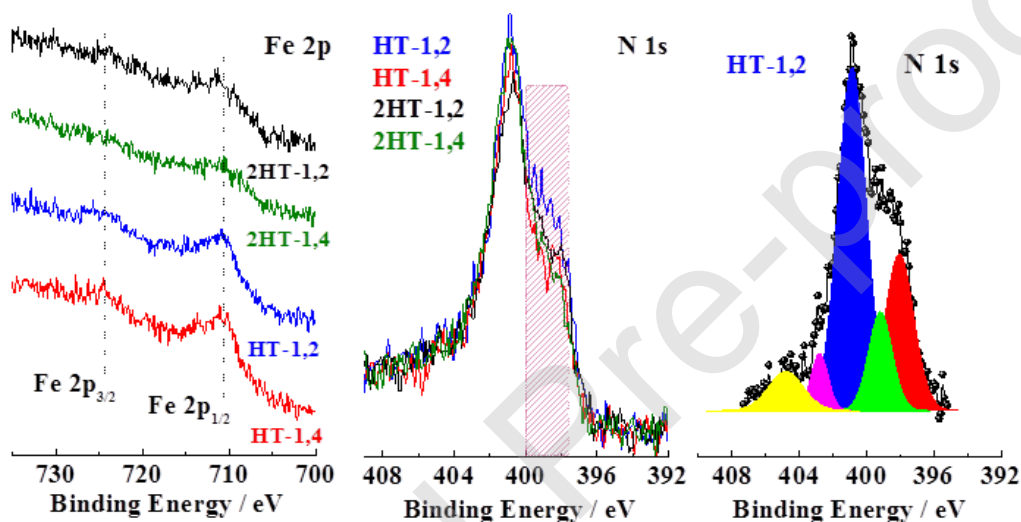


Figure 4: (a) Fe 2p and (b) N 1s core-level regions of the catalysts under study; the region where the FeN_x species appear is highlighted. (c) Deconvolution of the N 1s core-level region of HT-1,2 showing N-pyridinic (red peak), FeN_x (green peak), N-pyrrolic (blue peak), N-graphitic (magenta peak) and oxide (yellow peak).

The fraction of the N-species in each catalyst is reported in Table 2. As an example, Figure 4b illustrates how the spectrum for HT-1,2 is deconvoluted into 5 peaks. The highest fraction of N in FeN_x species (peak at ca. 399.2 eV) was found for HT-1,2, being ca. 14 %. By contrary, HT-1,4 shows the lowest fraction of N in FeN_x in the series of ca. 7 %. On the other hand, after acid leaching and the second pyrolysis step (2HT catalysts), both samples display a similar fraction of N atoms in FeN_x of ca. 10 %. These results indicate that the formation of FeN_x ensembles is favored when using 1,2-DBC as the C-N precursor probably because by being located in vicinal positions the N-bearing groups are more prone to coordinate to one Fe atom than the N-bearing groups in 1,4-DCB (see

Scheme 1). Nevertheless, the structure of the final catalysts, especially the 2HT catalysts, is strongly controlled by the thermal treatment, as deduced from the presence of N-groups in pyrrolic and pyridinic positions; in fact, pyrrolic-N is the most abundant N species in all catalysts, as shown in Table 2.

The oxidation state and environment of Fe atoms on both HT and 2HT samples have been further studied by XAS [44]. A Fe foil and Fe phthalocyanine (with Fe^{2+} coordinated to N in FeN_4) were used as standards. Figure 5a shows X-ray absorption near edge structure (XANES) edge and pre-edge regions of both HT samples compared with the standards. Both HT samples have a similar shape and XANES edge positions than Fe foil so, at least most of the Fe is zerovalent, in good agreement with the predominance of Fe and Fe_3C phases observed by XRD and TEM. The Fe short-range distances found for the HT samples in the Fourier transform (FT) from the Fe K-edge Extended X-ray absorption fine structure (EXAFS) signals (Figure 5b) appear in the same position (same distances) than those of Fe foil. Also, a decrease in the intensity of first shell Fe-Fe scattering signal with respect to Fe foil is visible in the FT and is confirmed also for higher coordination shells for both samples. This evolution can be explained as a combination of various effects: the decrease in the coordination numbers of Fe-Fe scattering as a consequence of particle size and the presence of other Fe species. It is also possible to notice a small signal at shorter distances, which could be explained with the existence of a small fraction of Fe-N species. This signal cannot be assigned with certainty because it is very low and close to the noise level but this assumption would be consistent with the XPS observations. Considering the signal intensity, the majority of Fe atoms are in metallic phase therefore the difference with respect to foil is ascribed mainly to particle size effect, suggesting the presence of Fe nanoparticles in both HT samples. A more accurate evaluation of particle size and of the signal ascribed to other Fe species (including FeN_x moieties) is not feasible because the two effects interfere.

The analysis of the XANES data of the 2HT catalysts (Figure 5c) reveals an obvious shift of the Fe K-edge towards larger energies for 2HT samples as compared to HT samples, indicating that Fe in 2HT samples is more oxidised than HT samples [50]. The XANES K-edges appear very close to that of Fe phthalocyanine, indicating the predominance of Fe atoms in 2+ oxidation state. However, it seems that the Fe atoms in the 2HT samples adopt a different geometry than that of Fe atoms in iron phthalocyanine. In the latter, a clear pre-peak is observed that does not appear in the spectra for the 2HT samples. This pre-peak is characteristic of Fe in the square-planar environment of Fe-N_4 ensembles [51].

The different pre-edge feature in 2HT indicates that the geometry of the Fe-N_x moieties in the 2HT catalysts is not the same as in Fe phthalocyanine. The different geometry can be related to the occupation of some of the axial empty positions of the square planar Fe-N₄ moieties, or to a bending of that moieties, as it has been reported elsewhere [52].

Regarding the FT-EXAFS of 2HT samples (Figure 5d), the bond length at short distance appears in a similar range than Fe-N in iron phthalocyanine, confirming that Fe distances in the 2HT catalysts correspond to an Fe-N coordination, and thus confirming the presence of FeN_x ensembles. Additionally, slight variations in the positions at the Fe-N shell are identified for the 2HT samples with respect to the Fe phthalocyanine standard, which may be explained by the different environment identified by XANES technique.

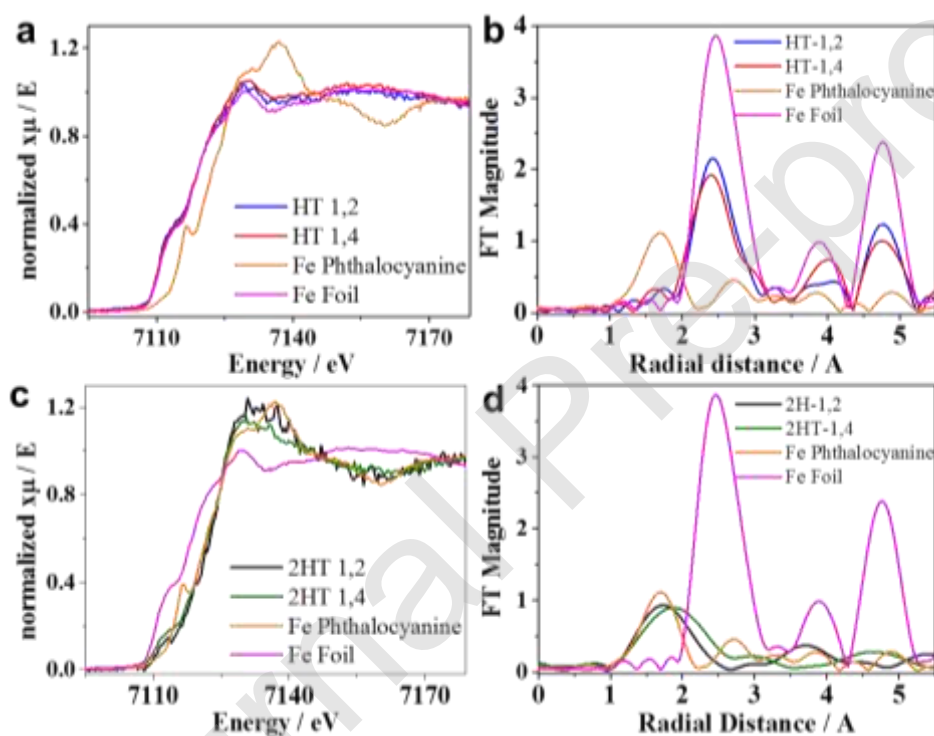


Figure 5: XAS results. a) Fe K-edge XANES spectra of HT samples. b) Fourier Transform of EXAFS signal for HT samples. c) Fe K-edge XANES spectra of 2HT samples. d) Fourier Transform of EXAFS signal for 2HT samples. Standards: Fe foil and Fe phthalocyanine.

Figure 6 shows the Raman spectra of the samples under study. Raman spectroscopy has been extensively used to analyze the structural defects of N-doped carbons. Graphitic compounds exhibit three characteristic bands at 1580 cm^{-1} (G band), 1351 cm^{-1} (D band) and 2700 cm^{-1} (2D band). The G band appears in all sp^2 carbons due to the stretching of C-C bond [53]. D and 2D bands indicate the degree of disorder on a carbon matrix [54].

The evolution of the intensity ratio between D and G bands (I_G/I_D) is usually monitored to assess the degree of disorder induced by the introduction of N (and Fe) in graphite-like samples (Inset to Figure 6) [55, 56].

The Raman spectra in the C region of all the samples under study and the I_D/I_G ratios are depicted in Figure 6. As observed, the samples show a similar $I_D/I_G \sim 1.02$ except for HT-1,4 which has a lower ratio of ca. 0.98. As shown in the study of the ORR catalytic performance discussed below, the presence of defects in the carbon could have a positive effect on the ORR activity [17]. In addition, HT-1,2 and both 2HT catalysts present a narrower D band than HT-1,4, which could be related to a higher fraction of defects on the carbon matrix, that can be related to a higher content of N inside the carbon matrix that incorporates imperfections in the carbon.[56] In fact, looking in detail to the Raman spectra, HT-1,4 is the sample with the broadest D band among all the catalysts.

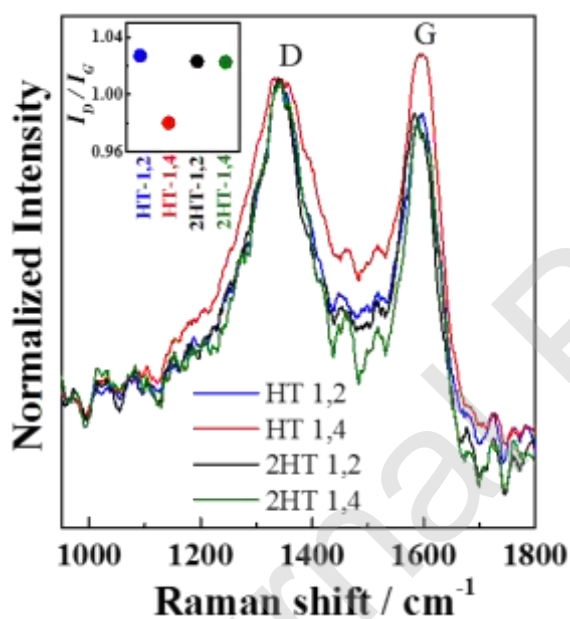


Figure 6: Raman spectra of the samples under study. Inset: Intensity ratio between D and G bands (I_G/I_D).

3.2 Electrocatalytic performance for the ORR in acid electrolyte

The ORR performance of the catalysts in acid media was evaluated using the thin film RDE approach. Faradaic currents were corrected from the background current recorded in Ar-saturated electrolytes (Fig. 7a). Figure 7c shows the current densities recorded during the ORR for HT and 2HT catalysts. In order to benchmark the ORR activity in

acid electrolyte the following parameters are usually measured; E_{onset} , $E_{1/2}$ and i_M . E_{onset} is defined as the potential at which a current density of 0.1 mA/cm^2 is achieved, $E_{1/2}$ is the half-wave potential, and i_M is the mass normalized kinetic current. The values obtained for each catalysts are collated in Table 3. As observed in Figure 7c, E_{onset} and $E_{1/2}$ potentials of the catalysts prepared with 1,2-DCB are slightly more positive than those of the catalysts based on 1,4-DCB. After the second thermal treatment, both E_{onset} and $E_{1/2}$ shift to slightly less positive potentials. HT-1,2 records the best E_{onset} of 0.86 V in the series whereas 2HT-1,2 records the most positive $E_{1/2}$ of 0.68 V. In Table 3, we compare the E_{onset} and $E_{1/2}$ values recorded by the DCB catalysts reported in this work, with those of representative catalysts reported in the literature. As observed, E_{onset} and $E_{1/2}$ values for the DCB catalysts are similar to those reported recently with similar Fe/N/C catalysts measured in acid electrolyte [37, 57-59] but lower than those reported for ZIF-based catalysts [60-62], which are the precursors rendering the most active catalysts for the ORR [20]. In any case, it should be also taken into account that the activities reported in Table 3 are for catalysts that have not been subjected to acid leaching and/or second thermal treatment [19, 27, 60-63], which renders more active catalysts. Finally, it should be also noted that most catalysts reported in Table 3 have not been subjected to AST, so their durability cannot be assessed. It is well accepted that catalysts displaying high activity usually display low durability, and *vice versa* [20]. In addition, a further advantage of the DCB catalysts vs the most active catalysts reported in Table 3 is that they have been prepared using expensive starting materials.

The higher ORR activity of the catalysts synthesized from 1,2-DCB is in line with the highest fraction of Fe-N_x moieties present in HT-1,2 and 2HT-1,2. As indicated above, it has been reported that FeN_x ensembles are the most active sites for the ORR at low overpotentials in this class of catalysts [43]. This line of reasoning also explains the lowest ORR activity of HT-1,4, which records lowest content of FeN_x and the highest fraction of pyrrolic-N in the series (see Table 2).

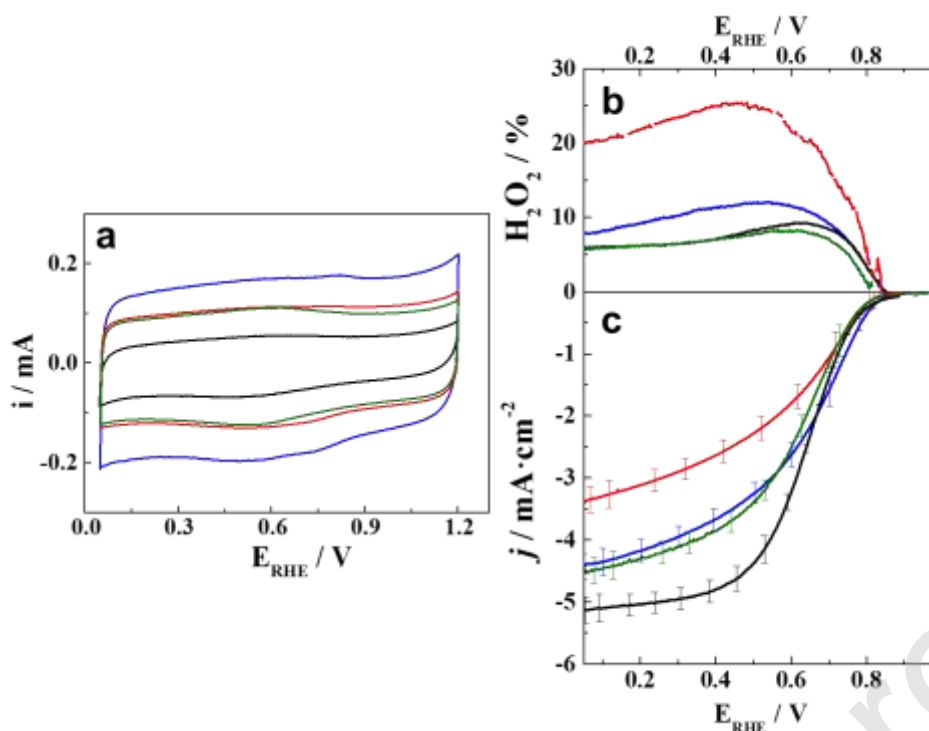


Figure 7: a) Cyclic voltammograms in 0.1 M HClO₄ at 10 mVs⁻¹ for HT-1,2 (blue), HT-1,4 (red), 2HT-1,2 (black), 2HT-1,4 (green). b) % H₂O₂ obtained during the ORR experiments. c) ORR polarization curves recorded at 10 mV s⁻¹ and 1600 rpm. The ORR measurements have been performed three times for each catalyst and the standard deviation has been included.

As also observed in Table 3, the E_{onset} potentials are not strongly affected by the acid leaching and second pyrolysis step, suggesting that the active sites responsible for the ORR activity at low overpotentials were already generated during the first pyrolysis treatment and also that these active sites are not soluble in acid electrolyte.

On the other hand, as observed in Figure 7c, the polarization curves of the catalysts subjected to acid leaching and second pyrolysis treatment record higher current densities, especially in the mixed and diffusional controlled regions.

Table 3. Mass activity and onset potentials for the ORR with the catalysts under study and some of the best catalysts reported.

Catalyst	E_{onset} (V) at -0.1 mA/cm ²	$E_{1/2}$ (V)	i_M (A/g) at 0.7 V	i_M (A/g) at 0.8 V
HT-1,2	0.86(1)	0.64(3)	4.0(2)	0.61(8)
HT-1,4	0.82(2)	0.61(2)	2.5(1)	0.34(8)
2HT-1,2	0.85(2)	0.670(3)	3.1(2)	0.43(8)
2HT-1,4	0.83(7)	0.630(1)	2.5(1)	0.32(6)

Fe-N/MPC1 [58]	0.81	0.68	~8.8*	~0.4*
Fe-N/MPC2 [58]	0.82	0.70	~6.2*	~0.6*
Fe-PEI-1 [59]	0.82	0.64	~2.5*	~0.3*
Fe-PEI-2 [59]	0.80	0.59	~1.8*	~0.2*
Mesoporous Fe-N-C [64]	-	0.73	-	0.8
LDH@ZIF-67-800 [60]	-	0.68	-	1.5
CPM-99(Fe)/C [63]	-	0.73	-	1.2
Fe-N/C-800 [65]	-	0.66	-	1.0
PFeTMPP-1000 [27]	-	0.75	-	2.5
CPANI-Fe-NaCl [66]	-	0.73	-	1.2
Fe/N/G [19]	-	0.72	-	1.2
FeIM/ZIF-8 [61]	-	0.76	-	6.5
Fe-PANI + DCDA [67]	-	0.83	-	8.6
Fe-N-C-Phen-PANI [68]	-	0.80	-	5.7
Fe0.5-950-ZIF [62]	-	0.89	-	120
Fe(2.0)/PI(100) [69]	-	0.77	-	7.4
(CM+PANI)-Fe-C [70]	-	0.80	-	9.0

The Tafel plots for the catalysts, calculated from the pure kinetic currents (mass transport corrected) are shown in Figure 8a. As observed, the Tafel plots for the HT samples go in parallel but are somehow different from that of the 2HT samples. 2HT-1,2 displays a single slope of 120 mV/decade within the whole polarization range (0.8-0.6 V). A similar pattern is observed for sample 2HT-1,4, a single Tafel slope of ca. 110 mV/decade is observed within the whole polarization range. On the other hand, an (over)potential dependence of the Tafel slope is found for the HT catalysts. Thus, in the low overpotential (LO) region, a Tafel slope between 60-70 mV/decade is found for HT-1,2 and HT-1,4. At higher overpotentials (HO; 0.7 - 0.6 V), Tafel slopes increases progressively to 120 mV/decade reaching a value ca. 240 mV/decade are found at high overpotentials suggesting a change of mechanism within this potential range with the HT-catalysts. Tafel slopes of 60 and 120 mV/decade for the ORR are the most typical ones reported at LO and HO, respectively [71, 72]. However, it is not unusual to find higher and lower Tafel slope values for Pt/C and/or Fe/N/C catalysts and in some cases, it can be observed a change in the Tafel with the potential [72-74]. The origin of the potential-dependence of the Tafel slope is still under debate; some authors ascribe it to changes in coverage, or site blocking effect [75, 76] whereas other authors sustain that changes in Tafel slope reflect intrinsic features of the ORR mechanism on Fe/N/C catalysts [73]. Our results

show that the ORR proceeds differently over the HT and the 2HT catalysts. Whereas the 2HT catalysts display a single Tafel slope of ca. 120 mV/decade, which is consistent with a single-electron transfer rate limiting, the HT samples display a clear potential-dependence Tafel slope. As discussed above, this feature could be ascribed to the presence of blocking species or to changes in reaction mechanism. It should be noted that, by not being subjected to acid leaching, different types of Fe species are present in the HT-catalysts, namely metallic Fe, iron oxides, Fe_3C , FeN_x , which could contribute to the overall ORR by promoting different reaction pathways.

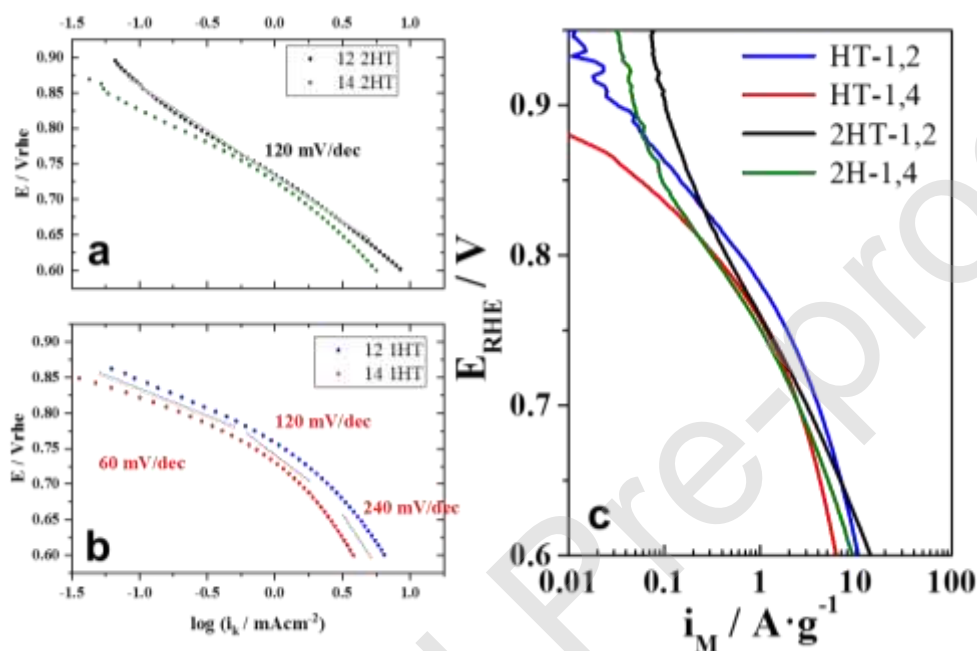


Figure 8. a) Tafel plots of 2HT catalysts b) Tafel plots of HT catalysts and c) mass currents (i_M) obtained from the pure kinetic currents.

In fact, the highest production of H_2O_2 is observed with the HT catalysts (Figure 7b). On the other hand, only FeN_x (and graphite-wrapped Fe_3C) species are the only Fe-containing species in the 2HT catalysts. As a result, the $4e^-$ pathway is favored over the 2HT catalysts (see below). The contribution of the $2e^-$ and $4e^-$ reaction pathways has been assessed by quantifying the production of H_2O_2 during the ORR by using a rotating ring disk electrode. RDDE experiments were conducted during the ORR by setting the Pt ring at 1.2 V to ensure the oxidation of H_2O_2 but avoiding the oxidation of H_2O . The amount of peroxide produced was determined from the following equation:

$$X_{\text{H}_2\text{O}_2} = \frac{2 \frac{i_R}{N}}{i_D + \frac{i_R}{N}} \quad \text{Eq. 1}$$

where ' i_D ' is the disk current and ' i_R ' is the ring current. N is the ring efficiency (26 %). The number of electrons transferred was calculated from the following equation:

$$n_e = 4 - \frac{\% H_2O_2}{50\%} \quad \text{Eq. 2}$$

Figure 7b shows the evolution of H_2O_2 production with the potential with the catalysts under study. As observed, the HT catalysts generate higher amounts of H_2O_2 during the ORR than the 2HT ones. Thus, HT-1,4 records the highest production of hydrogen peroxide of ca. 25 % at 0.5 V, which at least to some extent explains the lower limiting current achieved by this sample. HT-1,2 generates 12 % of H_2O_2 , and the 2HT samples around 7-8 %. These figures were taken at 0.5 V, which is the potential where the production of peroxide is expected to be maximum. As deduced from Eq. 2, the number of exchanged electrons during the ORR with the 2HT catalyst is of ~ 3.9 ; very close to the theoretical value of $4 e^-$ for the complete reduction of O_2 to H_2O .

A key parameter to define the ORR activity of Fe/N/C catalysts is the mass activity. Mass activities have been obtained from the pure kinetic currents obtained from mass-transport correction of the thin-film RDE currents using the Koutecky-Levich equation.

$$i_k = \frac{(-i_f \times i_{lim})}{i_f - i_{lim}} \quad \text{Eq. 3}$$

Where i_k is the kinetic current, which is negative for reduction reactions, and i_{lim} is the limiting current. The ORR mass activity is determined by the following formula:

$$i_m = \frac{i_k}{m_{cat}} \quad \text{Eq. 4}$$

Where m_{cat} is the loading of the catalyst on the electrode in grams.

Figure 8b show the mass activities (i_m) for the catalysts studied in this work and Table 3 reports i_m at 0.7 V and 0.8 V. As observed, the ORR mass activities of the catalysts obtained from the 1,2-DCB precursor are higher than that obtained with the 1,4-DCB counterpart. In fact, HT-1,2 shows the best onset potential and the highest i_m at 0.7 V and 0.8 V in the series. The mass activity of all catalysts decreases after acid washing and the second thermal treatment, especially that of the 1,2-DCB/Fe. The mass activities at 0.8 V are compared with state-of-the-art catalysts (Table 3). As it was commented for the current densities, the results obtained are similar or smaller than reported Fe/N/C catalysts; however, the strong point of our work is the novel approach we have found to

synthesize inexpensive Fe/N/C catalysts with very high durability and acceptable activity values on RDE and MEA (see below).

As deduced from the results above, the catalysts prepared using 1,2-DCB are the most active ones for the ORR. In order to analyze catalyst stability during the ORR, 2HT-1,2 was subjected to 5000 cycles at 50 mVs^{-1} between 0.6 and 1.0 V *vs.* RHE in Ar saturated electrolyte. Figure 9 shows the ORR polarization curves recorded before and after the durability test (AST) and the corresponding i_M plots.

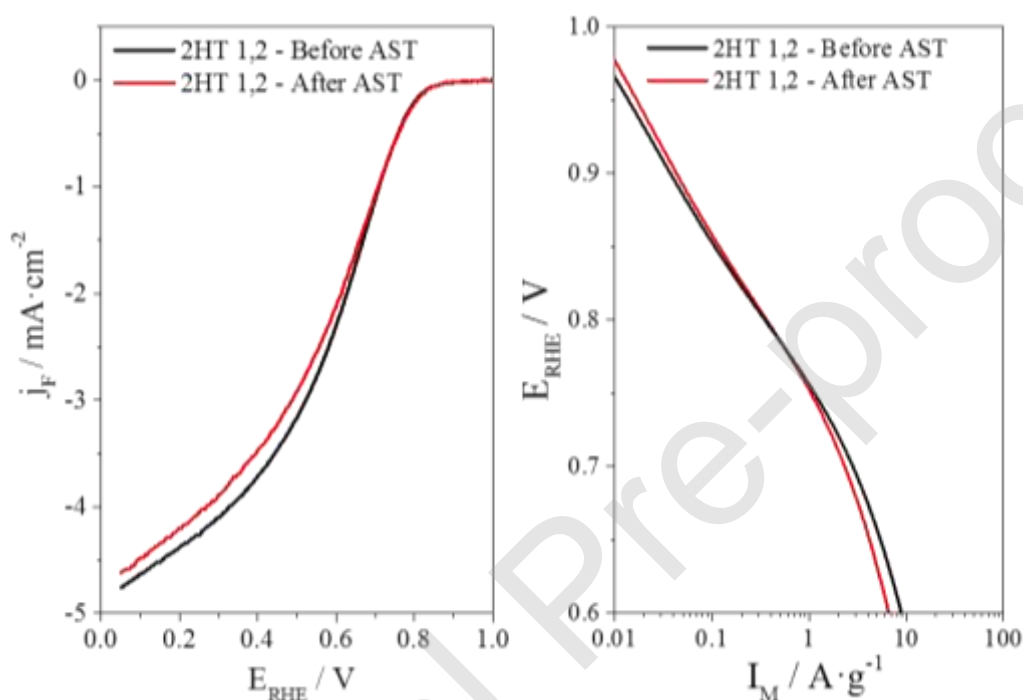


Figure 9: AST test for 2HT-1,2. 5000 cycles at 50 mVs^{-1} between 0.6 and 1.0 V in Ar saturated electrolyte. a) Current density before and after the AST test. b) Mass activity before and after the AST test.

As observed in Figure 9, 2HT-1,2 shows excellent durability and stability during the AST and the ORR polarization curves are almost identical, especially in the kinetic region. We observe a slight reduction of the limiting current after the AST due to the loss of active sites during several cycles of reaction in acid electrolyte (Figure 9a). This effect has been previously reported for similar Fe/N/C catalysts [15, 77-79]. The mass normalized ORR activity remains unchanged after the durability test, as observed in Figure 9b.

3.3 Single Cell Proof-of-Concept studies

A MEA was assembled by using 2HT as catalyst on the cathode side and carbon supported Platinum as catalyst on the anode side. The performance of the MEA was tested under H_2 and air conditions. For the anode the commercial Pt/C electrode with $0.3 \text{ mg}_{\text{Pt}}\text{cm}^{-2}$ loading was used and the catalyst loading of the cathode was $2.0 \text{ mg}_{1,2\text{-HTC}}\text{cm}^{-2}$. The MEA was pressed between two Graphite-Plates with 1 Nm cm^{-2} clamping pressure and was heated at 90°C for five minutes. The MEA was tested in a 1 cm^2 single cell hardware multichannel with 3 meanders made in graphite, compatible with the differential cell configuration at the testing stands of DLR (German Aerospace Center). A homemade bench test controlled by programmable logic controllers (PLC) was used, which allows for an automatic control of the input and output conditions, such as pressure, temperature, flow rate of gases, humidity of reactants. The relative humidity (RH) of the inlet gases was controlled through water-filled heated sparger bottles. The RH was 100% and the temperature of the cell was fixed at 80°C . Lines between humidifiers and the fuel cell were heated in order to avoid water condensation. The gas mass flow rates were regulated at the fuel cell inlets whereas the pressure was controlled at the outlets. The pressure was fixed for the experiment at constant value of 450 kPa. Gas flow was controlled through the test station and set constant under high stoichiometry to avoid starvation process and maintain the homogeneity.

Figure 10 shows the polarization and power density curves obtained at 80°C in the conditions above. Before discussing the results, it should be noted that we have studied the performance of the catalyst under less favorable, yet more relevant for the PEMFC community conditions, than usually reported in the literature. We have used a low catalyst loading ($2.0 \text{ mg}_{\text{cat}}\text{cm}^{-2}$ vs ca. $4 \text{ mg}_{\text{cat}}\text{cm}^{-2}$ or even more usually reported for the higher power densities in the literature [20]) and using air instead of oxygen as oxidant, the voltage were also presented without iR -free correction. These reaction conditions result in lower activities. In fact, establishing a proper comparison of the catalytic performance of Fe/N/C catalysts in single cells versus literature is difficult due to the wide range of the reaction conditions reported in the literature [20]. As observed in Figure 10, the open circuit voltage is around 800 mV and the maximum power density is ca. 70 mWcm^{-2} . This power value is similar to the average value obtained for non-ZIF derived Fe-based catalysts measured in H_2 /air fuel cells [20]. Therefore, our values are in line with the performances obtained for similar Fe/N/C catalysts [74] but lower than those reported for state-of-the-art fuel cells, although in those cases the results have been obtained using higher catalyst loadings and normally using O_2 instead of air as oxidant.

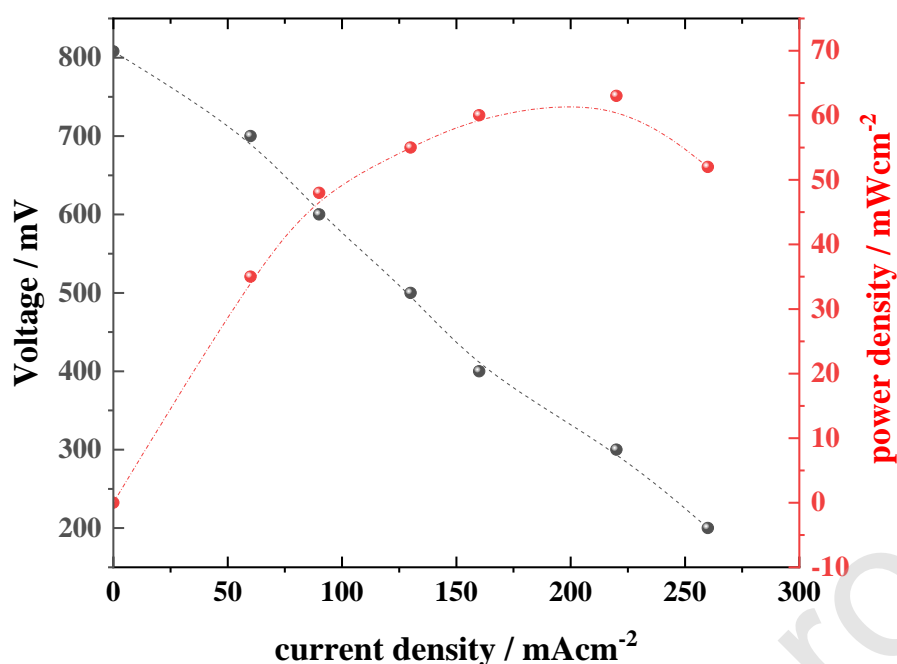


Figure 10: Polarization (black dots) and power density (red dots) curves obtained at 80°C, 100% RH at 450 kPa. Catalyst loading: 2.0 mgcm⁻² (2HT-1,2 as cathode) and 0.3 mgcm⁻² (Pt/C as anode). H₂ flow 50 mLmin⁻¹; Air flow 150 mLmin⁻¹.

In any case, the MEA results presented in this work clearly show that the Fe/N/C catalysts obtained from the pyrolysis of porous organic triazine precursors can be used under relevant conditions in a proton exchange membrane fuel cell. As shown in the RDE experiments, the catalysts reported in this work, especially 2HT-1,2 display high ORR activity and durability in acid electrolyte, and in MEA.

Conclusions

Fe/N/C catalysts for the oxygen reduction reaction in acid electrolyte have been prepared by pyrolysis of triazine porous organic polymer (TPOP) obtained by polymerization of inexpensive starting materials, DCBs in the presence of an iron precursors. The characterization analyses reveal that several iron species are stable in the catalysts after the first pyrolysis treatment. However only FeN_x and carbon-wrapped Fe₃C are stable after acid leaching and second pyrolysis. The position of the N-bearing groups of the monomer (DCB) used for the synthesis of the TPOP has a strong influence in the

formation of FeN_x moieties. FeN_x moieties promote the 4 e⁻ pathway of the ORR and are stable during the ORR in acid electrolyte.

Authors contribution

All authors contributed equally to the manuscript, more specifically

- Álvaro García prepared the catalysts, characterized the catalyst by RAMAN and conducted the ORR experiments
- María Retuerto supervised the experiments and contributed to the writing of the manuscript.
- Carlota Dominguez synthesized the catalysts and measured their ORR activity
- Laura Pascual characterized the catalysts by TEM and contributed to the writing of the manuscript
- Pilar Ferrer, Diego Gianolio and Aida Serrano conducted the XAS experiments
- Pia Assmann and Daniel G. Sanchez conducted the MEA testing
- Miguel A. Peña. Conducted ATG analysis
- Sergio Rojas Conceived and supervised the experiments. Conducted XPS analyses. Writing the article

Declaration of interests

☒ The authors declare that they have no known competing financial interests or personal relationships that could have appeared to influence the work reported in this paper.

Acknowledgements

This work was supported by PEGASUS project, funded by the European Union's Horizon 2020 Programme (call JTI-FCH-2017-1) for the Fuel Cells and Hydrogen Joint Technology Initiative under grant agreement n° 779550, and by project ENE2016-77055-C3-3-R from the Spanish Ministry of Economy and Competitiveness (MINECO). We acknowledge the Spanish CRG BM25-SpLine, MINECO, The Spanish National Research Council (CSIC) and The European Synchrotron (The ESRF) for provision of synchrotron radiation facilities.

References

- [1] I. Katsounaros, S. Cherevko, A.R. Zeradjanin, K.J.J. Mayrhofer, Oxygen Electrochemistry as a Cornerstone for Sustainable Energy Conversion, *Angew. Chem. Int. Ed.*, 53 (2014) 102-121.10.1002/anie.201306588.
- [2] V.R. Stamenkovic, D. Strmcnik, P.P. Lopes, N.M. Markovic, Energy and fuels from electrochemical interfaces, *Nat. Mater.*, 16 (2016) 57.10.1038/nmat4738.
- [3] H.A. Gasteiger, S.S. Kocha, B. Sompalli, F.T. Wagner, Activity benchmarks and requirements for Pt, Pt-alloy, and non-Pt oxygen reduction catalysts for PEMFCs, *Applied Catalysis B-Environmental*, 56 (2005) 9-35.10.1016/j.apcatb.2004.06.021.
- [4] O. Gröger, H.A. Gasteiger, J.-P. Suchsland, Review—Electromobility: Batteries or Fuel Cells?, *Journal of The Electrochemical Society*, 162 (2015) A2605-A2622.10.1149/2.0211514jes.
- [5] A. Kongkanand, M.F. Mathias, The Priority and Challenge of High-Power Performance of Low-Platinum Proton-Exchange Membrane Fuel Cells, *The Journal of Physical Chemistry Letters*, 7 (2016) 1127-1137.10.1021/acs.jpcclett.6b00216.
- [6] A. Serov, K. Artyushkova, E. Niangar, C. Wang, N. Dale, F. Jaouen, M.-T. Sougrati, Q. Jia, S. Mukerjee, P. Atanassov, Nano-structured non-platinum catalysts for automotive fuel cell application, *Nano Energy*, 16 (2015) 293-300.10.1016/j.nanoen.2015.07.002.
- [7] F. Jaouen, E. Proietti, M. Lefèvre, R. Chenitz, J.-P. Dodelet, G. Wu, H.T. Chung, C.M. Johnston, P. Zelenay, Recent advances in non-precious metal catalysis for oxygen-reduction reaction in polymer electrolyte fuelcells, *Energy Environ. Sci.*, 4 (2011) 114-130.10.1039/c0ee00011f.
- [8] M. Lefevre, E. Proietti, F. Jaouen, J.P. Dodelet, Iron-based catalysts with improved oxygen reduction activity in polymer electrolyte fuel cells, *Science*, 324 (2009) 71-74.10.1126/science.1170051.
- [9] G. Wu, K.L. More, C.M. Johnston, P. Zelenay, High-Performance Electrocatalysts for Oxygen Reduction Derived from Polyaniline, Iron, and Cobalt, *Science*, 332 (2011) 443-447.10.1126/science.1200832.
- [10] G. Wu, K.L. More, P. Xu, H.L. Wang, M. Ferrandon, A.J. Kropf, D.J. Myers, S. Ma, C.M. Johnston, P. Zelenay, A carbon-nanotube-supported graphene-rich non-precious metal oxygen reduction catalyst with enhanced performance durability, *Chem Commun (Camb)*, 49 (2013) 3291-3293.10.1039/c3cc39121c.
- [11] E. Proietti, F. Jaouen, M. Lefevre, N. Larouche, J. Tian, J. Herranz, J.P. Dodelet, Iron-based cathode catalyst with enhanced power density in polymer electrolyte membrane fuel cells, *Nat Commun*, 2 (2011) 416.10.1038/ncomms1427.
- [12] G. Wu, A. Santandreu, W. Kellogg, S. Gupta, O. Ogoke, H. Zhang, H.-L. Wang, L. Dai, Carbon nanocomposite catalysts for oxygen reduction and evolution reactions: From nitrogen doping to transition-metal addition, *Nano Energy*, 29 (2016) 83-110.10.1016/j.nanoen.2015.12.032.
- [13] A.A. Gewirth, J.A. Varnell, A.M. DiAscro, Nonprecious Metal Catalysts for Oxygen Reduction in Heterogeneous Aqueous Systems, *Chemical Reviews*, 118 (2018) 2313-2339.10.1021/acs.chemrev.7b00335.
- [14] L. Zhang, D.P. Wilkinson, Y. Liu, J. Zhang, Progress in nanostructured (Fe or Co)/N/C non-noble metal electrocatalysts for fuel cell oxygen reduction reaction, *Electrochimica Acta*, 262 (2018) 326-336.10.1016/j.electacta.2018.01.046.
- [15] Y. He, Q. Tan, L. Lu, J. Sokolowski, G. Wu, Metal-Nitrogen-Carbon Catalysts for Oxygen Reduction in PEM Fuel Cells: Self-Template Synthesis Approach to Enhancing Catalytic Activity and Stability, *Electrochemical Energy Reviews*, 2 (2019) 231-251.10.1007/s41918-019-00031-9.

- [16] L. Osmieri, Transition Metal–Nitrogen–Carbon (M–N–C) Catalysts for Oxygen Reduction Reaction. Insights on Synthesis and Performance in Polymer Electrolyte Fuel Cells, *ChemEngineering*, 3 (2019).10.3390/chemengineering3010016.
- [17] C. Domínguez, F.J. Pérez-Alonso, M. Abdel Salam, S.A. Al-Thabaiti, A.Y. Obaid, A.A. Alshehri, J.L. Gómez de la Fuente, J.L.G. Fierro, S. Rojas, On the relationship between N content, textural properties and catalytic performance for the oxygen reduction reaction of N/CNT, *Applied Catalysis B: Environmental*, 162 (2015) 420-429.10.1016/j.apcatb.2014.07.002.
- [18] C. Domínguez, F.J. Pérez-Alonso, M. Abdel Salam, J.L. Gómez De La Fuente, S.A. Al-Thabaiti, S.N. Basahel, M.A. Peña, J.L.G. Fierro, S. Rojas, Effect of transition metal (M: Fe, Co or Mn) for the oxygen reduction reaction with non-precious metal catalysts in acid medium, *International Journal of Hydrogen Energy*, 39 (2014) 5309-5318.10.1016/j.ijhydene.2013.12.078.
- [19] C. Dominguez, F.J. Perez-Alonso, M.A. Salam, S.A. Al-Thabaiti, M.A. Pena, F.J. Garcia-Garcia, L. Barrio, S. Rojas, Repercussion of the carbon matrix for the activity and stability of Fe/N/C electrocatalysts for the oxygen reduction reaction, *Applied Catalysis B-Environmental*, 183 (2016) 185-196.10.1016/j.apcatb.2015.10.043.
- [20] M. Shao, Q. Chang, J.P. Dodelet, R. Chenitz, Recent Advances in Electrocatalysts for Oxygen Reduction Reaction, *Chem Rev*, 116 (2016) 3594-3657.10.1021/acs.chemrev.5b00462.
- [21] M. Iefèvre, J.-P. Dodelet, Recent Advances in Non-Precious Metal Electrocatalysts for Oxygen Reduction in PEM Fuel Cells, *ECS Transactions*, 45 (2012) 35-44.10.1149/1.3701967.
- [22] F. Jaouen, M. Lefèvre, J.-P. Dodelet, M. Cai, Heat-Treated Fe/N/C Catalysts for O₂ Electroreduction: Are Active Sites Hosted in Micropores?, *The Journal of Physical Chemistry B*, 110 (2006) 5553-5558.10.1021/jp057135h.
- [23] R. Chenitz, U.I. Kramm, M. Lefevre, V. Glibin, G. Zhang, S. Sun, J.-P. Dodelet, A specific demetalation of Fe-N₄ catalytic sites in the micropores of NC_Ar + NH₃ is at the origin of the initial activity loss of the highly active Fe/N/C catalyst used for the reduction of oxygen in PEM fuel cells, *Energy & Environmental Science*, (2018).10.1039/C7EE02302B.
- [24] A. Monteverde Videla, D. Sebastián, N. Vasile, L. Osmieri, A. Aricò, V. Baglio, S. Specchia, Performance analysis of Fe–N–C catalyst for DMFC cathodes: Effect of water saturation in the cathodic catalyst layer, *International Journal of Hydrogen Energy*, 41 (2016).10.1016/j.ijhydene.2016.06.060.
- [25] S.J. Normile, D.C. Sabarirajan, O. Calzada, V. De Andrade, X. Xiao, P. Mandal, D.Y. Parkinson, A. Serov, P. Atanassov, I.V. Zenyuk, Direct observations of liquid water formation at nano- and micro-scale in platinum group metal-free electrodes by operando X-ray computed tomography, *Materials Today Energy*, 9 (2018) 187-197.10.1016/j.mtener.2018.05.011.
- [26] J. Shui, C. Chen, L. Grabstanowicz, D. Zhao, D.-J. Liu, Highly efficient nonprecious metal catalyst prepared with metal–organic framework in a continuous carbon nanofibrous network, *Proceedings of the National Academy of Sciences*, 112 (2015) 10629-10634.10.1073/pnas.1507159112.
- [27] S. Yuan, J.-L. Shui, L. Grabstanowicz, C. Chen, S. Commet, B. Reprogel, L. Yu, D.-J. Liu, A Highly Active and Support-Free Oxygen Reduction Catalyst Prepared from Ultrahigh-Surface-Area Porous Polyporphyrin, *Angewandte Chemie (International ed. in English)*, 52 (2013).10.1002/anie.201302924.

- [28] M. Chokai, T. Daidou, Y. Nabae, Development of Pt-Free Carbon-Based Catalyst for PEFC Cathode Prepared from Polyacrylonitrile, *ECS Transactions*, 64 (2014) 261-270.10.1149/06403.0261ecst.
- [29] M. Shao, Q. Chang, J.-P. Dodelet, R. Chenitz, Recent Advances in Electrocatalysts for Oxygen Reduction Reaction, *Chemical Reviews*, 116 (2016) 3594-3657.10.1021/acs.chemrev.5b00462.
- [30] S.K. Das, X. Wang, Z. Lai, Facile synthesis of triazine-triphenylamine-based microporous covalent polymer adsorbent for flue gas CO₂ capture, *Microporous and Mesoporous Materials*, 255 (2018) 76-83.<https://doi.org/10.1016/j.micromeso.2017.07.038>.
- [31] K. Sakaushi, M. Antonietti, Carbon- and Nitrogen-Based Organic Frameworks, *Acc Chem Res*, 48 (2015) 1591-1600.10.1021/acs.accounts.5b00010.
- [32] M. Yang, X. Long, H. Li, H. Chen, P. Liu, Porous Organic-Polymer-Derived Nitrogen-Doped Porous Carbon Nanoparticles for Efficient Oxygen Reduction Electrocatalysis and Supercapacitors, *ACS Sustainable Chemistry & Engineering*, 7 (2019) 2236-2244.10.1021/acssuschemeng.8b04919.
- [33] I.Y. Kim, S. Kim, X. Jin, S. Premkumar, G. Chandra, N.-S. Lee, G.P. Mane, S.-J. Hwang, S. Umapathy, A. Vinu, Ordered Mesoporous C₃N₅ with a Combined Triazole and Triazine Framework and Its Graphene Hybrids for the Oxygen Reduction Reaction (ORR), *Angewandte Chemie*, 57 (2018) 17135-17140.[doi:10.1002/anie.201811061](https://doi.org/10.1002/anie.201811061).
- [34] J.-D. Yi, R. Xu, G.-L. Chai, T. Zhang, K. Zang, B. Nan, H. Lin, Y.-L. Liang, J. Lv, J. Luo, R. Si, Y.-B. Huang, R. Cao, Cobalt single-atoms anchored on porphyrinic triazine-based frameworks as bifunctional electrocatalysts for oxygen reduction and hydrogen evolution reactions, *Journal of Materials Chemistry A*, 7 (2019) 1252-1259.10.1039/C8TA09490J.
- [35] W. Yu, S. Gu, Y. Fu, S. Xiong, C. Pan, Y. Liu, G. Yu, Carbazole-decorated covalent triazine frameworks: Novel nonmetal catalysts for carbon dioxide fixation and oxygen reduction reaction, *Journal of Catalysis*, 362 (2018) 1-9.<https://doi.org/10.1016/j.jcat.2018.03.021>.
- [36] A.-d. Tan, Y.-f. Wang, Z.-y. Fu, P. Tsiakaras, Z.-x. Liang, Highly effective oxygen reduction reaction electrocatalysis: Nitrogen-doped hierarchically mesoporous carbon derived from interpenetrated nonporous metal-organic frameworks, *Applied Catalysis B: Environmental*, 218 (2017) 260-266.<https://doi.org/10.1016/j.apcatb.2017.06.051>.
- [37] J.-D. Yi, R. Xu, Q. Wu, T. Zhang, K.-T. Zang, J. Luo, Y.-L. Liang, Y.-B. Huang, R. Cao, Atomically Dispersed Iron-Nitrogen Active Sites within Porphyrinic Triazine-Based Frameworks for Oxygen Reduction Reaction in Both Alkaline and Acidic Media, *ACS Energy Letters*, 3 (2018) 883-889.10.1021/acsenenergylett.8b00245.
- [38] P. Kuhn, M. Antonietti, A. Thomas, Porous, covalent triazine-based frameworks prepared by ionothermal synthesis, *Angew Chem Int Ed Engl*, 47 (2008) 3450-3453.10.1002/anie.200705710.
- [39] K. Schwinghammer, S. Hug, M.B. Mesch, J. Senker, B.V. Lotsch, Phenyl-triazine oligomers for light-driven hydrogen evolution, *Energy & Environmental Science*, 8 (2015) 3345-3353.10.1039/c5ee02574e.
- [40] P. Kuhn, M. Antonietti, A. Thomas, Porous, Covalent Triazine-Based Frameworks Prepared by Ionothermal Synthesis, *Angew. Chem. Int. Ed. Engl.*, 47 (2008) 3450-3453.[doi:10.1002/anie.200705710](https://doi.org/10.1002/anie.200705710).
- [41] B. Ravel, M. Newville, Athena, Artemis, Hephaestus: data analysis for X-ray absorption spectroscopy using IFEFFIT, *J Synchrotron Radiat*, 12 (2005) 537-541.
- [42] K. Artyushkova, A. Serov, S. Rojas-Carbonell, P. Atanassov, Chemistry of Multitudinous Active Sites for Oxygen Reduction Reaction in Transition Metal-

- Nitrogen–Carbon Electrocatalysts, *The Journal of Physical Chemistry C*, 119 (2015) 25917-25928.10.1021/acs.jpcc.5b07653.
- [43] F.J. Perez-Alonso, C. Dominguez, S.A. Al-Thabaiti, A.O. Al-Youbi, M.A. Salam, A.A. Alshehri, M. Retuerto, M.A. Pena, S. Rojas, Evidences of the presence of different types of active sites for the oxygen reduction reaction with Fe/N/C based catalysts, *Journal of Power Sources*, 327 (2016) 204-211.10.1016/j.jpowsour.2016.07.050.
- [44] Q. Jia, N. Ramaswamy, U. Tylus, K. Strickland, J. Li, A. Serov, K. Artyushkova, P. Atanassov, J. Anibal, C. Gumeci, S.C. Barton, M.-T. Sougrati, F. Jaouen, B. Halevi, S. Mukerjee, Spectroscopic insights into the nature of active sites in iron–nitrogen–carbon electrocatalysts for oxygen reduction in acid, *Nano Energy*, 29 (2016) 65-82.<http://dx.doi.org/10.1016/j.nanoen.2016.03.025>.
- [45] Q. Jia, N. Ramaswamy, H. Hafiz, U. Tylus, K. Strickland, G. Wu, B. Barbiellini, A. Bansil, E.F. Holby, P. Zelenay, S. Mukerjee, Experimental Observation of Redox-Induced Fe–N Switching Behavior as a Determinant Role for Oxygen Reduction Activity, *ACS Nano*, 9 (2015) 12496-12505.10.1021/acs.nano.5b05984.
- [46] D. Guo, R. Shibuya, C. Akiba, S. Saji, T. Kondo, J. Nakamura, Active sites of nitrogen-doped carbon materials for oxygen reduction reaction clarified using model catalysts, *Science*, 351 (2016) 361-365.10.1126/science.aad0832.
- [47] J.A. Behan, A. Iannaci, C. Domínguez, S.N. Stamatina, M.K. Hoque, J.M. Vasconcelos, T.S. Perova, P.E. Colavita, Electrocatalysis of N-doped carbons in the oxygen reduction reaction as a function of pH: N-sites and scaffold effects, *Carbon*, 148 (2019) 224-230.<https://doi.org/10.1016/j.carbon.2019.03.052>.
- [48] H.T. Chung, D.A. Cullen, D. Higgins, B.T. Sneed, E.F. Holby, K.L. More, P. Zelenay, Direct atomic-level insight into the active sites of a high-performance PGM-free ORR catalyst, *Science*, 357 (2017) 479-484.10.1126/science.aan2255.
- [49] I. Matanovic, K. Artyushkova, P. Atanassov, Understanding PGM-free catalysts by linking density functional theory calculations and structural analysis: Perspectives and challenges, *Current Opinion in Electrochemistry*, 9 (2018) 137-144.10.1016/j.coelec.2018.03.009.
- [50] J. Rubio-Zuazo, A. Chainani, M. Taguchi, D. Malterre, A. Serrano, G.R. Castro, Electronic structure of FeO, γ -Fe₂O₃, and Fe₃O₄ epitaxial films using high-energy spectroscopies, *Physical Review B*, 97 (2018) 235148.10.1103/PhysRevB.97.235148.
- [51] M.C.M. Alves, J.P. Dodelet, D. Guay, M. Ladouceur, G. Tourillon, Origin of the electrocatalytic properties for oxygen reduction of some heat-treated polyacrylonitrile and phthalocyanine cobalt compounds adsorbed on carbon black as probed by electrochemistry and x-ray absorption spectroscopy, *The Journal of Physical Chemistry*, 96 (1992) 10898-10905.10.1021/j100205a054.
- [52] H. Fei, J. Dong, Y. Feng, C.S. Allen, C. Wan, B. Voloskiy, M. Li, Z. Zhao, Y. Wang, H. Sun, P. An, W. Chen, Z. Guo, C. Lee, D. Chen, I. Shakir, M. Liu, T. Hu, Y. Li, A.I. Kirkland, X. Duan, Y. Huang, General synthesis and definitive structural identification of MN₄C₄ single-atom catalysts with tunable electrocatalytic activities, *Nature Catalysis*, 1 (2018) 63-72.10.1038/s41929-017-0008-y.
- [53] M.S. Dresselhaus, A. Jorio, M. Hofmann, G. Dresselhaus, R. Saito, Perspectives on Carbon Nanotubes and Graphene Raman Spectroscopy, *Nano Letters*, 10 (2010) 751-758.10.1021/nl904286r.
- [54] P. Delhaes, M. Couzi, M. Trinquécoste, J. Dentzer, H. Hamidou, C. Vix-Guterl, A comparison between Raman spectroscopy and surface characterizations of multiwall carbon nanotubes, *Carbon*, 44 (2006) 3005-3013.10.1016/j.carbon.2006.05.021.

- [55] H. Wang, T. Maiyalagan, X. Wang, Review on Recent Progress in Nitrogen-Doped Graphene: Synthesis, Characterization, and Its Potential Applications, *ACS Catalysis*, 2 (2012) 781-794.10.1021/cs200652y.
- [56] L.G. Bulusheva, A.V. Okotrub, I.A. Kinloch, I.P. Asanov, A.G. Kurennya, A.G. Kudashov, X. Chen, H. Song, Effect of nitrogen doping on Raman spectra of multi-walled carbon nanotubes, *physica status solidi (b)*, 245 (2008) 1971-1974.10.1002/pssb.200879592.
- [57] U. Tylus, Q. Jia, H. Hafiz, R.J. Allen, B. Barbiellini, A. Bansil, S. Mukerjee, Engendering anion immunity in oxygen consuming cathodes based on Fe-Nx electrocatalysts: Spectroscopic and electrochemical advanced characterizations, *Applied Catalysis B: Environmental*, 198 (2016) 318-324.<https://doi.org/10.1016/j.apcatb.2016.05.054>.
- [58] L. Osmieri, R. Escudero-Cid, M. Armandi, A.H.A. Monteverde Videla, J.L. García Fierro, P. Ocón, S. Specchia, Fe-N/C catalysts for oxygen reduction reaction supported on different carbonaceous materials. Performance in acidic and alkaline direct alcohol fuel cells, *Applied Catalysis B: Environmental*, 205 (2017) 637-653.<https://doi.org/10.1016/j.apcatb.2017.01.003>.
- [59] A. Serov, U. Tylus, K. Artyushkova, S. Mukerjee, P. Atanassov, Mechanistic studies of oxygen reduction on Fe-PEI derived non-PGM electrocatalysts, *Applied Catalysis B: Environmental*, 150-151 (2014) 179-186.<https://doi.org/10.1016/j.apcatb.2013.12.009>.
- [60] Z. Li, M. Shao, L. Zhou, R. Zhang, C. Zhang, M. Wei, D.G. Evans, X. Duan, Directed Growth of Metal-Organic Frameworks and Their Derived Carbon-Based Network for Efficient Electrocatalytic Oxygen Reduction, *Adv Mater*, 28 (2016) 2337-2344.10.1002/adma.201505086.
- [61] S.H. Ahn, X. Yu, A. Manthiram, "Wiring" Fe-Nx-Embedded Porous Carbon Framework onto 1D Nanotubes for Efficient Oxygen Reduction Reaction in Alkaline and Acidic Media, *Advanced Materials*, 29 (2017) 1606534.10.1002/adma.201606534.
- [62] A. Zitolo, V. Goellner, V. Armel, M.T. Sougrati, T. Mineva, L. Stievano, E. Fonda, F. Jaouen, Identification of catalytic sites for oxygen reduction in iron- and nitrogen-doped graphene materials, *Nat Mater*, 14 (2015) 937-942.10.1038/nmat4367.
- [63] Q. Lin, X. Bu, A. Kong, C. Mao, X. Zhao, F. Bu, P. Feng, New heterometallic zirconium metalloporphyrin frameworks and their heteroatom-activated high-surface-area carbon derivatives, *J Am Chem Soc*, 137 (2015) 2235-2238.10.1021/jacs.5b00076.
- [64] A. Kong, X. Zhu, Z. Han, Y. Yu, Y. Zhang, B. Dong, Y. Shan, Ordered Hierarchically Micro- and Mesoporous Fe-Nx-Embedded Graphitic Architectures as Efficient Electrocatalysts for Oxygen Reduction Reaction, *ACS Catalysis*, 4 (2014) 1793-1800.10.1021/cs401257j.
- [65] L. Lin, Q. Zhu, A.-W. Xu, Noble-Metal-Free Fe-N/C Catalyst for Highly Efficient Oxygen Reduction Reaction under Both Alkaline and Acidic Conditions, *Journal of the American Chemical Society*, 136 (2014) 11027-11033.10.1021/ja504696r.
- [66] W. Ding, L. Li, K. Xiong, Y. Wang, W. Li, Y. Nie, S. Chen, X. Qi, Z. Wei, Shape Fixing via Salt Recrystallization: A Morphology-Controlled Approach To Convert Nanostructured Polymer to Carbon Nanomaterial as a Highly Active Catalyst for Oxygen Reduction Reaction, *J Am Chem Soc*, 137 (2015) 5414-5420.10.1021/jacs.5b00292.
- [67] S. Gupta, S. Zhao, O. Ogoke, Y. Lin, H. Xu, G. Wu, Engineering Favorable Morphology and Structure of Fe-N-C Oxygen-reduction Catalysts via Tuning Nitrogen/Carbon Precursors, *ChemSusChem*, 10 (2016).10.1002/cssc.201601397.
- [68] X. Fu, P. Zamani, J.-Y. Choi, F.M. Hassan, G. Jiang, D.C. Higgins, Y. Zhang, M.A. Hoque, Z. Chen, In Situ Polymer Graphenization Ingrained with Nanoporosity in a Nitrogenous Electrocatalyst Boosting the Performance of Polymer-Electrolyte-

- Membrane Fuel Cells, *Advanced Materials*, 29 (2017) 1604456.10.1002/adma.201604456.
- [69] Y. Nabee, Morphology-Controlled Nitrogen-Containing Polymers as Synthetic Precursors for Electrochemical Oxygen Reduction Fe/N/C Cathode Catalysts, *Catalysts*, 8 (2018) 324.10.3390/catal8080324.
- [70] H. Chung, D. Cullen, D. Higgins, B. Sneed, E. Holby, K. More, P. Zelenay, Direct atomic-level insight into the active sites of a high-performance PGM-free ORR catalyst, *Science*, 357 (2017) 479-484.10.1126/science.aan2255.
- [71] J.H. Zagal, M.T.M. Koper, Reactivity Descriptors for the Activity of Molecular MN₄ Catalysts for the Oxygen Reduction Reaction, *Angewandte Chemie International Edition*, 55 (2016) 14510-14521.10.1002/anie.201604311.
- [72] T. Shinagawa, A.T. Garcia-Esparza, K. Takanabe, Insight on Tafel slopes from a microkinetic analysis of aqueous electrocatalysis for energy conversion, *Scientific Reports*, 5 (2015) 13801.10.1038/srep13801.
- [73] J. Chlistunoff, RRDE and Voltammetric Study of ORR on Pyrolyzed Fe/Polyaniline Catalyst. On the Origins of Variable Tafel Slopes, *The Journal of Physical Chemistry C*, 115 (2011) 6496-6507.10.1021/jp108350t.
- [74] L. Osmieri, R. Escudero-Cid, A.H.A. Monteverde Videla, P. Ocón, S. Specchia, Performance of a Fe-N-C catalyst for the oxygen reduction reaction in direct methanol fuel cell: Cathode formulation optimization and short-term durability, *Applied Catalysis B: Environmental*, 201 (2017) 253-265.https://doi.org/10.1016/j.apcatb.2016.08.043.
- [75] N.M. Marković, P.N. Ross, Surface science studies of model fuel cell electrocatalysts, *Surface Science Reports*, 45 (2002) 117-229.10.1016/S0167-5729(01)00022-X.
- [76] J. Li, A. Alsudairi, Z.-F. Ma, S. Mukerjee, Q. Jia, Asymmetric Volcano Trend in Oxygen Reduction Activity of Pt and Non-Pt Catalysts: In Situ Identification of the Site-Blocking Effect, *Journal of the American Chemical Society*, 139 (2017) 1384-1387.10.1021/jacs.6b11072.
- [77] B.J. Kim, D.U. Lee, J. Wu, D. Higgins, A. Yu, Z. Chen, Iron- and Nitrogen-Functionalized Graphene Nanosheet and Nanoshell Composites as a Highly Active Electrocatalyst for Oxygen Reduction Reaction, *The Journal of Physical Chemistry C*, 117 (2013) 26501-26508.10.1021/jp410014a.
- [78] R. Jäger, P.E. Kasatkin, E. Härk, P. Teppor, T. Romann, R. Härmas, I. Tallo, U. Mäeorg, U. Joost, P. Paiste, K. Kirsimäe, E. Lust, The effect of N precursors in Fe-N/C type catalysts based on activated silicon carbide derived carbon for oxygen reduction activity at various pH values, *Journal of Electroanalytical Chemistry*, 823 (2018) 593-600.10.1016/j.jelechem.2018.06.040.
- [79] D. Banham, S. Ye, K. Pei, J.-i. Ozaki, T. Kishimoto, Y. Imashiro, A review of the stability and durability of non-precious metal catalysts for the oxygen reduction reaction in proton exchange membrane fuel cells, *Journal of Power Sources*, 285 (2015) 334-348.10.1016/j.jpowsour.2015.03.047.